J Mater Sci (2009) 44:3975–3982
DOI 10.1007/s10853-009-3542-4

Nanotubular oxide layer formation on Ti–13Nb–13Zr alloy as a function of applied potential

Viswanathan S. Saji · Han Cheol Choe · William A. Brantley

Received: 6 March 2009 / Accepted: 2 May 2009 / Published online: 21 May 2009

Abstract Nanotubular oxide layer formation on biomedical grade $\alpha + \beta$ type Ti–13Nb–13Zr alloy was investigated using anodization technique as a function of applied dc potential (10–40 V) and anodizing time (30–180 min) in 1 M H_3PO_4 + 0.5 wt% NaF at room temperature. The as-formed and crystallized nanotubes were characterized using SEM, XRD, and TEM. There was a bimodal size distribution of nanotubes with diameters at the range of 25–110 nm. Nanotubes nucleated on β matrix exhibited uniform surface appearance with circular morphology, whereas those nucleated on α phase yielded parabolic shape. TEM/EDS analysis detected the three component elements of the alloy in the nanotube. Heat treatment significantly altered the distinct interface between the nanotubes and the barrier oxide layer.

Introduction

It has been shown that the formation of ordered oxide nanotubes on titanium alloys can increase the osseointegration of an implant material [1, 2]. Electrochemical anodization technique under optimized conditions is an efficient and economic approach for the production of self-ordered nanotubular structure on biometals [3, 4]. Such nanostructure formations have been achieved electrochemically on Ti-, Zr-, Nb-, and Ta-like valve metals [5–7]. Anodization of Ti and Zr resulted in distinctly separate hollow cylinder shaped nanotubes; however, porous oxide layers resulted in the case of Nb and Ta [5]. In a recently reported work, high aspect ratio tantalum oxide nanotube arrays were fabricated via one-step anodization of Ta foil [8]. Nanotube growth has been reported on binary, ternary, and quaternary titanium alloys such as TiNb, TiZr, Ti–6Al–7Nb, and Ti–29Nb–13Ta–4Zr [5]. In the anodization of Ti, the dissolution is enhanced by fluoride containing electrolytes, by forming soluble complexes with titanium resulting in pore or nanotube formation [5, 9]. Optimized parameters such as anodization potential, nature of the electrolyte, concentration of the electrolyte, temperature, and the potential sweep rate is critical in achieving self-ordered nanotubes.

In vitro studies showed that nanotubular titania surface provides a favorable template for the growth of bone cells [10]. The cells cultured on nanotubular surface showed higher adhesion, proliferation, alkaline phosphate activity, and bone matrix deposition compared to those grown on flat titanium surfaces. Their in vivo biocompatibility results suggested that nanotubular titania does not cause chronic inflammation or fibrosis [10]. The increased effective surface area and the introduction of anatase form of TiO_2 in the nanotubes after a proper heat treatment can further improve the biological activity [11]. Under these perspectives, nanotubular oxide layer formation on titanium alloys by anodization possesses importance in potential implant applications.

Ti–13Nb–13Zr alloy [12] has been widely investigated for biomedical implant applications, due to its excellent biocompatibility and mechanical properties like low elastic modulus. A low rigidity titanium alloy decreases the elastic modulus difference between the bone (10–30 GPa) and the implant material, thereby promoting load sharing between

V. S. Saji · H. C. Choe (✉)
Department of Dental Materials, School of Dentistry, Chosun University, Gwangju 501-759, Korea
e-mail: hcchoe@chosun.ac.kr

W. A. Brantley
College of Dentistry, The Ohio State University, Columbus, OH 43210, USA

them [13]. Insufficient load sharing may cause natural bone resorption and loosening of the joint [14].

When compared to titanium alloys having single phase microstructure; achieving homogeneously ordered nanotubular oxide layer formation on dual phase microstructure is difficult. Selective dissolution of less stable elements or different reaction rates of different alloy phases can hinder nanotube formation. Also, no reported information is available on nanotubular oxide layer formation on Ti–13Nb–13Zr alloy. Hence, in this study, we investigated nanotubular oxide formation on the alloy as a function of applied dc potential and time of anodization in electrolyte containing 1 M H_3PO_4 and 0.5 wt% NaF. The as-formed and crystallized nanotubes were characterized using SEM, XRD, and TEM.

Experimental

Ti–13Nb–13Zr alloy was fabricated by arc melting with nonconsumable tungsten electrode and water cooled copper hearth under ultrapure argon atmosphere. Commercially high pure Ti, Nb, Ta, and Zr were employed. All the ingots were melted and inverted 10 times in order to homogenize the alloy chemical composition. To homogenize the microstructure, the casted alloy was heat treated at 1000 °C for 2 h in Ar atmosphere, followed by water quenching. The phase structure and chemical composition of the heat-treated alloy were identified by X-ray diffraction (XRD, X'pert Pro, Philips, Netherlands) using a Cu-kα radiation and energy dispersive X-ray spectroscopy (EDS, JXA-8900M, JEOL, Japan), respectively. Chemical etching was performed using Keller's reagent ($HF + HCl + HNO_3 + H_2O$) and the microstructure was observed using scanning electron microscope (FE-SEM Hitachi 4800, Japan). The chemical composition of the alloy as determined by EDS was Ti:Nb:Zr = 72.38:13.58:14.04.

A two-electrode system consisting of platinum as the counter electrode and the working electrode as anode was used for anodization. A dc power source (Agilent E 3641 A) was employed for the purpose. The sample was mounted on a cold mount epoxy resin. Before anodization, the sample was polished by standard ANSI silicon carbide papers of different grades ranging from 100 to 2000 and finally alumina polished (1 μm), ultrasonically cleaned in deionised water and dried in flowing nitrogen. The electrolyte used was 1 M H_3PO_4 + 0.5 wt% NaF. The area of the sample exposed was 1 cm^2. The anodization was performed by increasing the potential of the sample from 0 V to the desired potential (10–40 V) with a scan rate of 100 mV s^{-1}, followed by holding the sample at the potential for a desired time (30–180 min). The anodized samples were rinsed by de-ionized water and dried in air. FE-SEM was used for observing the surface, lateral and bottom view images of the nanotubes. The cross-sectional and bottom views were taken from mechanically scratched samples.

The as-formed nanotubular alloy was subjected to heat treatment at two selected temperatures, viz. 150 and 350 °C for 120 min with a view to understand their crystallization behavior as well as to study the effect of heat treatment on the nanotubes/barrier oxide interface. A tubular furnace was employed for the purpose. The heating rate used was 5 °C/min. The phase structure of the as-formed and the heat-treated nanotubular alloy was examined by XRD using a Cu-kα radiation. Transmission electron microscope (FE-TEM/EDS, JEM-2100F, JEOL, Japan) was employed to observe the nanotube structure more precisely. A focused ion beam miller (FIB, SMI3050SE, Seiko Instruments, Japan) was used for specimen preparation for TEM studies.

Results and discussion

Phase and microstructure of Ti–13Nb–13Zr alloy

A representative SEM image of Ti–13Nb–13Zr alloy is shown in Fig. 1. The alloy exhibits $\alpha + \beta$ microstructure with acicular martensite phases. An XRD analysis revealed peaks corresponding to both α and β phases. Peaks corresponding to α' martensite were not detected in the XRD pattern; may be because of low concentration.

Nanotube formation as a function of applied dc potential

Figure 2 presents the surface and lateral view SEM images of the nanotubular oxide layer formed on the alloy when the anodization time was 60 min. At lower anodizing

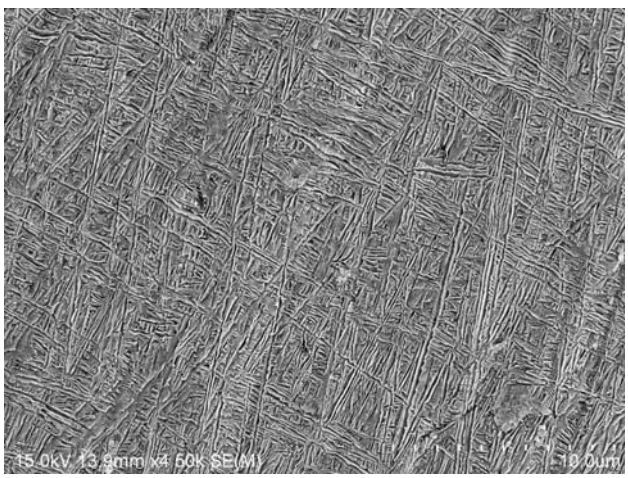

Fig. 1 Typical SEM microstructure of Ti–13Nb–13Zr alloy

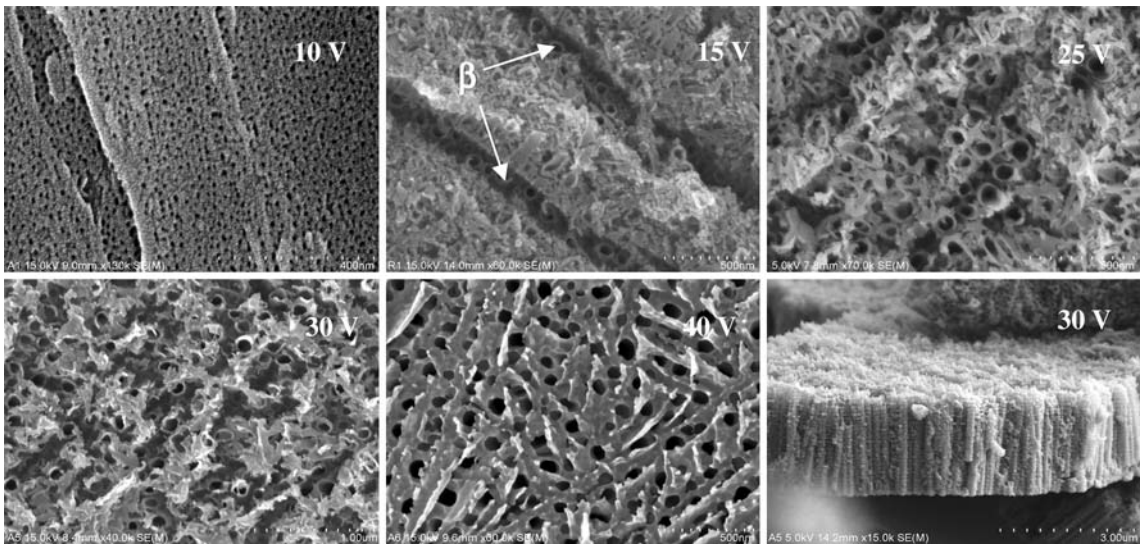

Fig. 2 SEM surface and lateral view images as a function of applied potential; time of anodization was 60 min

potential (10 V), the oxide layer formed possess a spongy-porous appearance with pore sizes at the range of 10–20 nm. At a higher applied potential (40 V), compact porous oxide layer having pore sizes at the range of 50–100 nm was formed. Nanotubular oxide layer formation was observed in the potential range of 15–30 V. The lateral view image implies that the nanotubes formed were highly ordered. Figure 3 represents the corresponding SEM images when the anodization time was 120 min. Nanotubular oxide layer formation was observed at all the applied potentials in the range of 10–25 V except at 15 V. At 15 V, the alloy exhibited a porous outer structure. When the time of anodization was increased to 180 min (Fig. 4), nanotubular oxide layer formation was observed at all the applied potentials in the range of 10–25 V. However, at 30 V, compact porous oxide layer resulted. It is clear from the figures that the most desirable potential range for nanotubular oxide layer formation was 20–25 V, irrespective of the anodization time. Also, it can be noticed that the nanotubular layer formed was irregular in surface appearance, irrespective of the applied potential and time of anodization.

Initiation of nanotube formation is preceded by nanopore formation. The porous structure obtained at 15 V in the present study (Fig. 3) can be explained based on the mechanism put forward by Tsuchiya et al. [15]. The nanoporous oxide structure formed under lower applied potentials and anodization time may possess a two layer

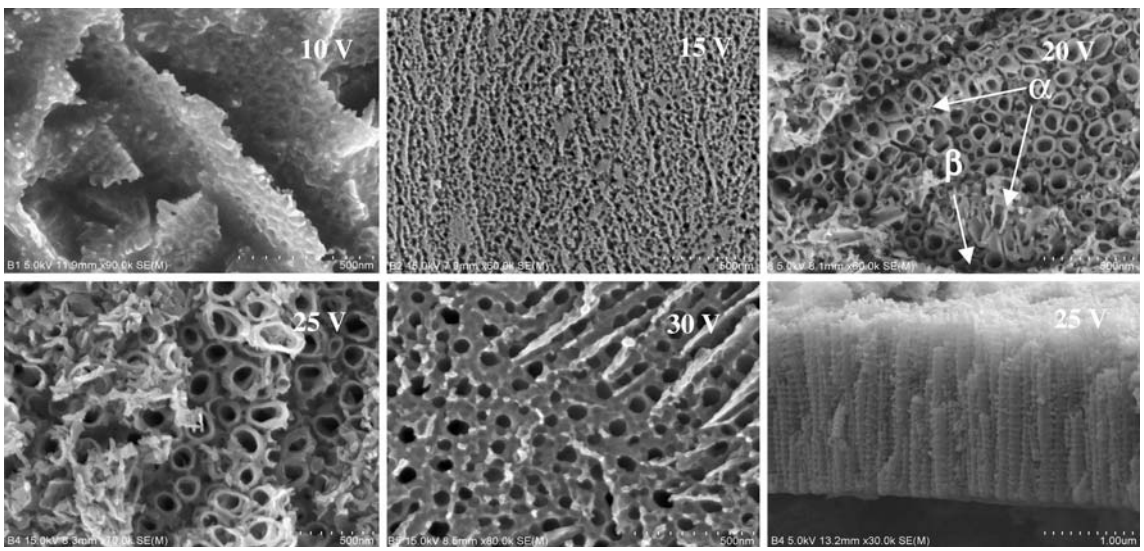

Fig. 3 SEM surface and lateral view images as a function of applied potential; time of anodization was 120 min

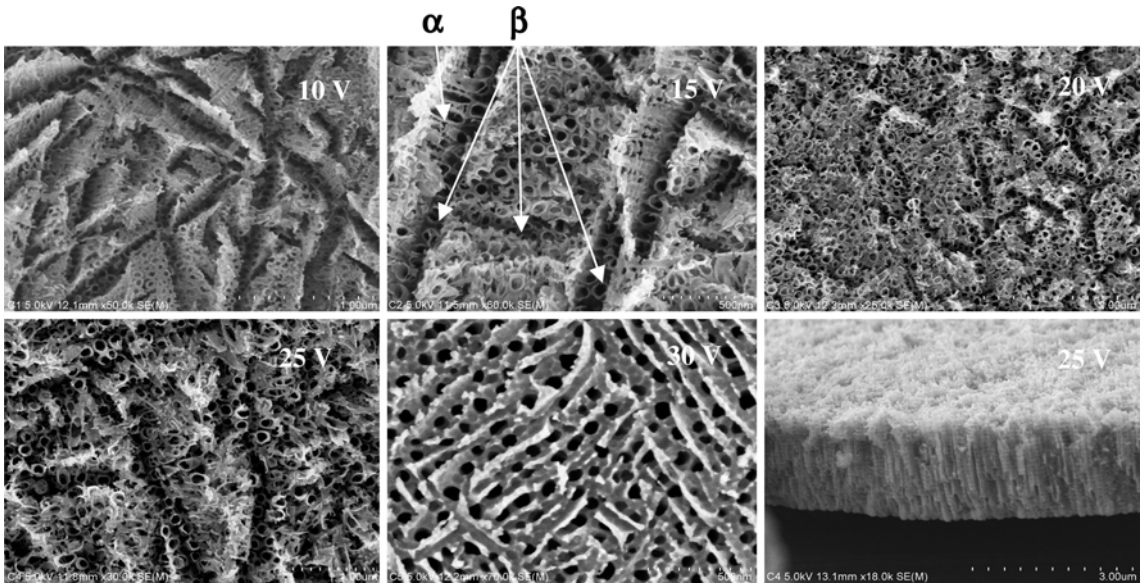

Fig. 4 SEM surface and lateral view images as a function of applied potential; time of anodization was 180 min

structure, i.e. outer nanoporous layer and inner nanotubular layer. With increase in anodization time and potential, the top nanoporous layer is completely dissolved revealing the underlying nanotubular layer [15]. It should be noted that the top veiw of the nanotubular layer formed at 10 V (Fig. 3) and 15 V (Fig. 2) does not show fully developed nanotubes all throughout the surface. With extended time of anodization, nanotube formation can be achieved even below the critical potential [15].

Figure 5 shows the typical bottom view images of the nanotubes formed. There was a bimodal size distribution of nanotubes. The diameters of the tubes vary in the range of 25–110 nm. The average diameter of the smallest and largest nanotubes increased from 25 nm and 60 nm to 40 nm and 110 nm, respectively, when the applied potential was increased from 10 to 25 V. Reported studies showed that nanotube pore size in F^- containing electrolyte is proportional to the applied potential and independent of anodization time and the electrolyte concentration [16]. The average length of the nanotubes formed was ~ 2 μm. The variation in the length of the nanotubes observed with increase in anodization time and potential was marginal. In strongly acidic solutions (pH < 1), both the nanotube growth rate and dissolution rate are increased, therefore increasing the anodization time does not increase the nanotube length [16]. The unwanted precipitates formed on the nanotubes may be associated with the higher pH of the electrolyte [16]. The dual phase microstructure of the alloy may also assist in the precipitate formation. Our EDS analysis showed that these precipitates were rich in Ti (~ 35 wt%) and P (~ 10 wt%), and balance elemental oxygen. The presence of P on the nanotubes may be favorable in osseointegration. Figures 6 and 7 more clearly explains the nanotube surface morphology in selected areas of the alloy surface when the applied anodization potentials were 10 and 20 V, respectively.

The surface irregularity of the nanotubular layer may be attributed to the $\alpha + \beta$ dual microstructure of the alloy. When the alloy has a dual phase microstructure, one phase could get etched preferentially by the electrolyte. α phase

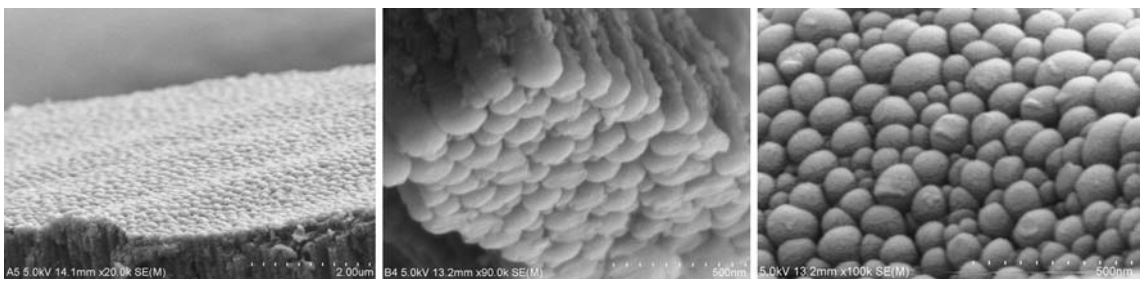

Fig. 5 SEM bottom view images of the nanotubular oxide layer

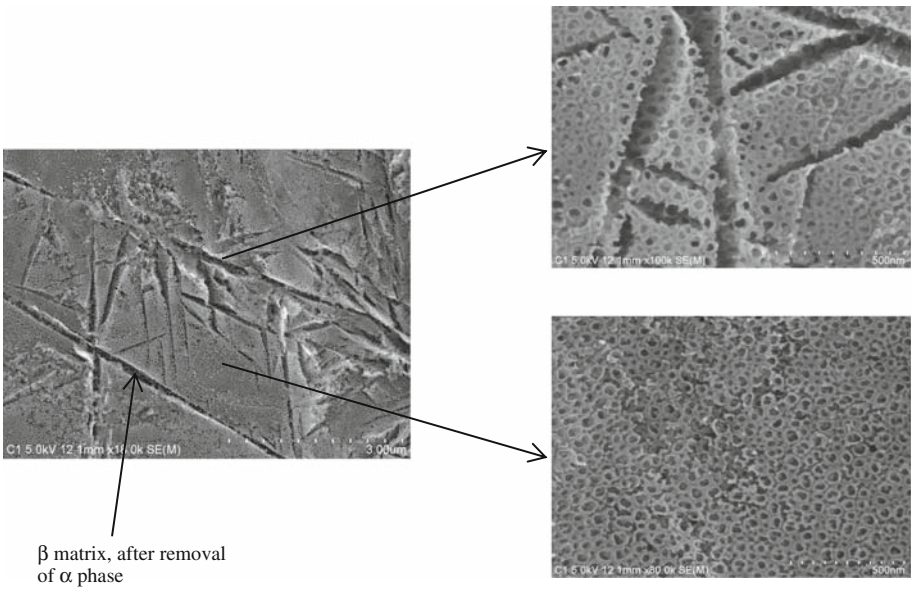

Fig. 6 Different surface view images of the nanotubes formed at 10 V; time of anodization was 180 min

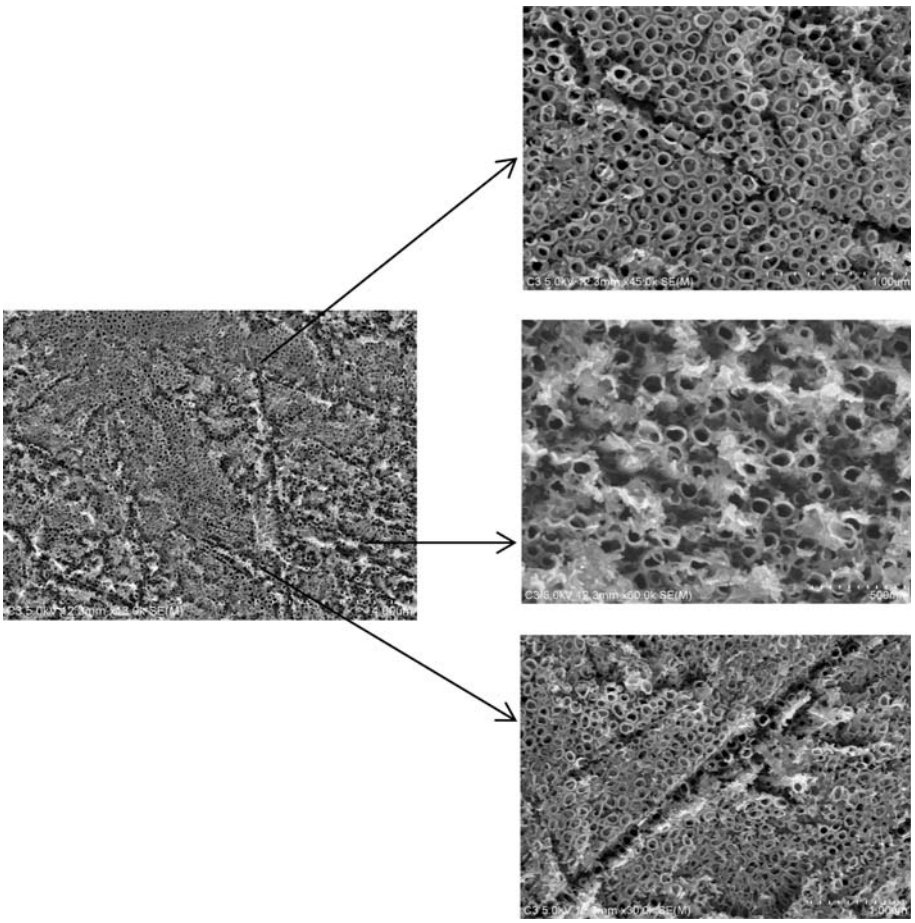

Fig. 7 Different surface view images of the nanotubes formed at 20 V; time of anodization was 180 min

may suffer complete or partial dissolution during the initial stage of anodization in the acidic electrolyte. This preferential dissolution might have resulted in the nonuniform surface morphology of the nanotubular layer. From Figs. 2, 3, 4, 5, 6, and 7, it is evident that the nanotubes nucleated on β matrix possess uniform surface appearance with circular morphology. However, nanotubes nucleated at orthorhombic martensite phases yielded parabolic shape. The acicular phases seem to have affected overall nucleation and growth of nanotubes. However, the bottom view

images (Fig. 5) indicate that the nanotubes were nucleated all throughout the surface, irrespective of the phase. Zwilling et al. on Ti–6Al–4V alloy reported that irrespective of the applied voltage, the porosity diameter was dependent on the underlying phase. The diameters of the pores formed are of smaller dimension on top of the β phase than on top of α phase [17]. A nanopatterned implant surface may favor controlled cell growth, increased osteoblast adhesion and proliferation. The enhanced protein and cell binding capacities is attributed to the larger surface areas/roughness degrees and altered surface energies [18]. The irregular surface appearance of the nanotubular oxide layer formed on the present alloy may not affect the cell behavior significantly. However, more studies are needed in this direction.

The mechanism of nanotubular growth has been satisfactorily explained by different groups [5, 16, 19]. Uniform titania nanotube arrays of various pore sizes (20–100 nm), lengths (200–6000 nm), and wall thickness (7–35 nm) can be grown by controlled anodization in F^- containing acidic electrolytes. Higher current densities were observed in anodization sweep when the electrolyte contained F^- ions [5, 16]. This was attributed to the additional chemical oxide dissolution due to the formation of soluble TiF_6^{2-} fluoride complexes. The nanotube formation is controlled by both the anodic oxide formation and the subsequent leaching of the oxide layer as the water soluble TiF_6^{2-} fluoride complexes. This complex formation at the metal oxide/electrolyte interface prevents the possible metal hydroxide precipitation. With increase in growth time, the diffusion of fluoride ions to the tube bottom or transport of the formed fluorine complexes becomes rate determining. Under an optimized condition, the initial nanopores formed, equally share the available current and that might have resulted in the formation of self-ordered nanotubes. Such a process may occur when the pore growth rate is equal to the leaching/dissolution rate [5].

Crystallization behavior and nanotubes/barrier oxide interface morphology

Figure 8 shows the XRD pattern recorded at normal angle for the heat-treated nanotubular alloy. The as-formed (not shown here) as well as the heat-treated nanotubular alloy at 150 °C exhibited only the peaks corresponding to the $\alpha + \beta$ alloy, which probably indicate amorphous nature of the nanotubes. After the heat treatment at 350 °C, peaks corresponding to anatase phase of TiO_2 were detected. The crystallization behavior of nanotubular oxide layer formed on the present alloy was similar to that of pure titanium [16]. The crystallization of such nanotubes occurs in anatase phase at a temperature near 300 °C, and rutile phase starts appearing at around 500 °C, with the rutile phase dominating in nanotubes annealed at 700 °C. As it was difficult to detect the presence of Zr and Nb oxides in the nanotubes through XRD, we have carried out TEM/EDS analysis of the as-formed and heat-treated nanotubes. Table 1 represents the chemical composition of 12 selected portions of the as-formed nanotubes. The TEM/EDS analysis detected all the three constituent elements of the alloy in the nanotubes.

Figure 9a represents the TEM image of the as-formed nanotubular alloy. The bimodal size distribution of the nanotubes is apparent in the TEM image. As the figure illustrates, existence of a distinct interface between the nanotubes and the barrier oxide layer is evident. An

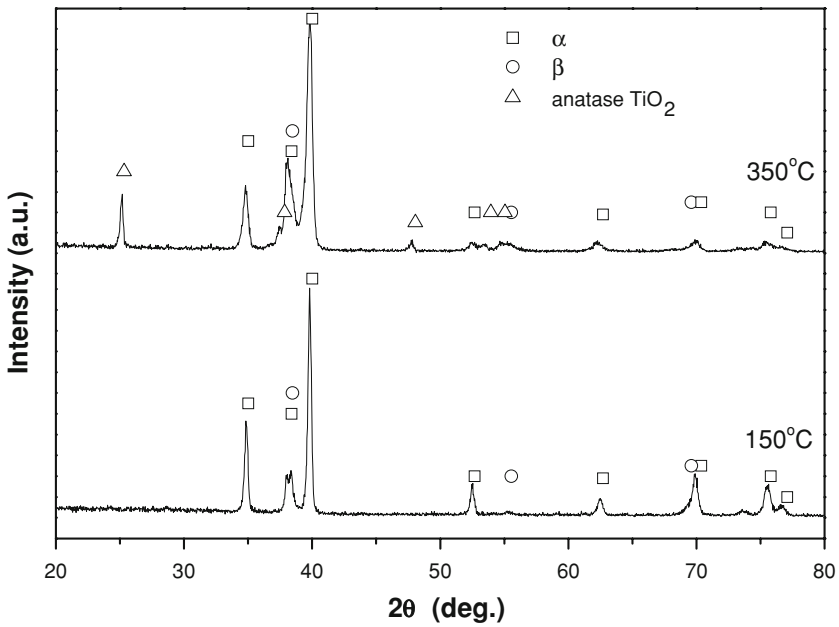

Fig. 8 XRD pattern of heat-treated nanotubular alloy at 150 and 350 °C

Table 1 TEM/EDS analysis of nanotubes (in wt%)

Spectrum	O	Ti	Zr	Nb
1	18.24	60.88	9.52	11.36
2	14.42	57.29	11.27	17.02
3	22.71	59.41	9.94	7.94
4	17.92	57.60	12.76	11.72
5	15.42	58.38	11.48	14.72
6	17.81	58.99	11.06	12.14
7	19.26	61.88	8.40	10.46
8	16.77	59.06	11.06	13.11
9	17.82	57.84	11.38	12.96
10	15.58	61.97	8.37	14.08
11	19.82	62.43	8.11	9.64
12	23.64	62.02	9.07	5.27

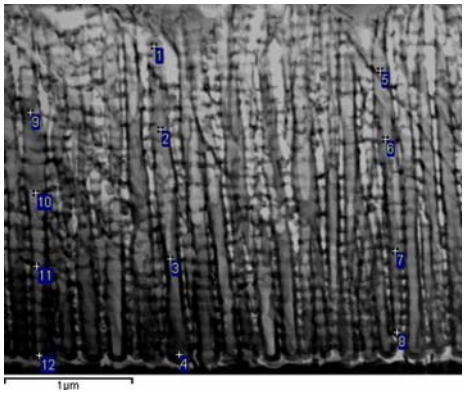

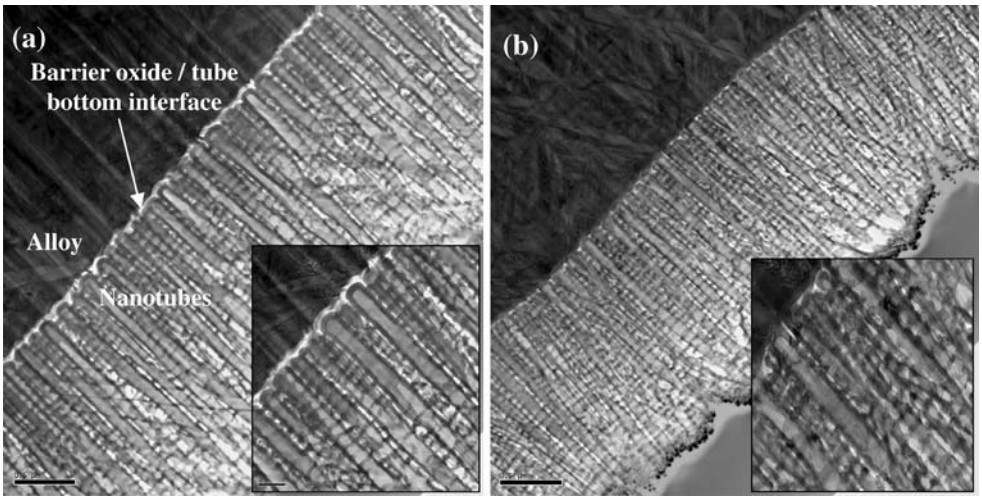

Fig. 9 TEM images of nanotubes **a** as formed and **b** after heat treatment [20]

expanded view of the interface region is also shown in the figure. The corresponding image after heat treatments is shown in Fig. 9b. It can be noted that the distinct interface was disintegrated after the heat treatment. The interface between the barrier oxide layer and the nanotubes gets fused to certain extent. Such an observation is important in view of ion dissolution behavior of nanotubular titanium alloys in body fluid. Ion dissolution behavior determines the biocompatibility of an implant. A suitable heat treatment may have significant effect on the biocompatibility of nanotubular titanium alloys.

Conclusions

Nanotubular oxide layer formation on $\alpha + \beta$ type Ti–13Nb–13Zr alloy was studied as a function of applied dc potential and anodization time in 1 M H_3PO_4 + 0.5 wt% NaF at room temperature. The most desirable potential range for nanotubular oxide formation was 20–25 V, irrespective of the anodization time. There was a bimodal size distribution of nanotubes with diameters at the range of 25–110 nm. Nanotubes nucleated on β matrix exhibited more regular surface morphology when compared to those nucleated on α phase. TEM/EDS analysis detected the three component elements of the alloy in the nanotubes. Heat treatment significantly altered the nanotubes/barrier oxide interface morphology.

References

1. Kubota S, Johkura K, Asanuma K, Okouchi Y, Ogiwara N, Sasaki K, Kasuga T (2004) J Mater Sci Mater Med 15:1031
2. Oh SH, Finõnes RR, Daraio C, Chen LH, Jin S (2005) Biomaterials 26:4938

3. Masuda H, Fukuda K (1995) Science 268:1466
4. Gong D, Grimes CA, Varghese OK, Hu WC, Sing RS, Chen Z, Dickey EC (2001) J Mater Res 16:3331
5. Macak JM, Tsuchiya H, Ghicov A, Yasuda K, Hahn R, Bauer S, Schmuki P (2007) Curr Opin Solid State Mater Sci 11:3
6. Elsanousi A, Zhang J, Fadlalla HMH, Zhang F, Wang H, Ding X, Huang Z, Tang C (2008) J Mater Sci 43:7219. doi:10.1007/s10853-008-2947-9
7. Tian T, Xiao XF, Liu RF, She HD, Hu XF (2007) J Mater Sci 42:5539. doi:10.1007/s10853-006-1104-6
8. Allam NK, Feng XJ, Grimes CA (2008) Chem Mater 20:6477
9. Jakubowics J (2008) Electrochem Commun 10:735
10. Popat KC, Leoni L, Grimes CA, Desai TA (2007) Biomaterials 28:3188
11. Uchida M, Kim HM, Kokubo T, Fujibayashi S, Nakamura T (2003) J Biomed Mater Res 64:164
12. Davidson JA, Kovacs P (1992) US Patent 4,169,597
13. Long M, Rack RJ (1998) Biomaterials 19:1621
14. Sumner DR, Galante JO (1992) Clin Orthoped Rel Res 274:202
15. Tsuchiya H, Macak JM, Ghicov A, Tang YC, Fujimoto S, Niinomi M, Noda T, Schmuki P (2006) Electrochim Acta 52:94
16. Mor GK, Varghese OK, Paulose M, Shankar K, Grimes CA (2006) Sol Energy Mater Sol Cells 90:2011
17. Zwilling V, Ceretti ED, Forveille AB (1999) Electrochim Acta 45:921
18. Jäger M, Zilkens C, Zanger K, Krauspe R (2007) J Biomed Biotechnol 2007:1
19. Bai J, Zhou B, Li L, Liu Y, Zheng Q, Shao J, Zhu X, Cai W, Liao J, Zou L (2008) J Mater Sci 43:1880. doi:10.1007/s10853-007-2418-8
20. Saji VS, Choe HC (2009) Corros Sci. doi:10.1016/j.corsci.2009.04.013